Davide Bigoni · Angelo Carini
Massimiliano Gei · Alberto Salvadori *Editors*

Fracture Phenomena in Nature and Technology

Proceedings of the IUTAM Symposium on Fracture Phenomena in Nature and Technology held in Brescia, Italy, 1–5 July 2012

Springer

Fracture Phenomena in Nature and Technology

Davide Bigoni • Angelo Carini
Massimiliano Gei • Alberto Salvadori
Editors

Fracture Phenomena in Nature and Technology

Proceedings of the IUTAM Symposium on Fracture Phenomena in Nature and Technology held in Brescia, Italy, 1–5 July 2012

Reprinted from *International Journal of Fracture*, Volume 184, Nos. 1–2 (2013)

Springer

Editors
Davide Bigoni
Massimiliano Gei
Dipartimento di Ingegneria Civile,
Ambientale e Meccanica
Università di Trento
Trento
Italy

Angelo Carini
Alberto Salvadori
Dipartimento di Ingegneria Civile,
Architettura, Territorio,
Ambiente e di Matematica
Università di Brescia
Brescia
Italy

ISBN 978-3-319-04396-8 ISBN 978-3-319-04397-5 (eBook)
DOI 10.1007/978-3-319-04397-5
Springer Cham Heidelberg New York Dordrecht London

Library of Congress Control Number: 2014936174

Printed on acid-free paper

Springer is part of Springer Science+Business Media (www.springer.com)

Contents

DOI 10.1007/978-3-319-04397-5_1
Reprinted from *International Journal of Fracture*, DOI 10.1007/s10704-013-9896-2

Foreword

D. Bigoni · A. Carini · M. Gei · A. Salvadori

Published online: 25 October 2013

This Special Issue of the International Journal of Fracture contains selected papers presented at the IUTAM Symposium *Fracture Phenomena in Nature and Technology* that was held at the School of Engineering, University of Brescia, Italy, during the week of July 1–5, 2012. The symposium focused on innovative contributions in fracture research, interpreted broadly to include new engineering and structural mechanics treatments of damage development and crack growth, large-scale failure processes as exemplified by earthquake or landslide failures, ice shelf break-up, and hydraulic fracturing (natural, or for resource extraction or CO_2 sequestration), small-scale rupture phenomena in materials physics including inception of shear banding, void growth, adhesion and decohesion in contact and friction, crystal dislocation processes, and atomic/electronic scale treatment of brittle crack tips and fundamental cohesive properties. The Special Issue manuscripts were limited to original work and were reviewed following the standard procedures of the Journal. The Organizing Committee is grateful to the IUTAM that fostered and supported the symposium, to the financial support from the EU (PIAP-GA-2011-286110-INTERCER2), to the University of Brescia (Italy) and to the University of Trento (Italy) that contributed greatly to the success of the Conference, to the Municipality of Brescia that welcomed the event and the participants.

Guest Editors

D. Bigoni (✉) · A. Carini · M. Gei · A. Salvadori
Trento, Italy
e-mail: bigoni@ing.unitn.it

DOI 10.1007/978-3-319-04397-5_2
Reprinted from *International Journal of Fracture*, DOI 10.1007/s10704-012-9788-x

ORIGINAL PAPER

Modeling fracture by material-point erosion

A. Pandolfi · B. Li · M. Ortiz

Received: 3 August 2012 / Accepted: 6 November 2012 / Published online: 20 November 2012

Abstract The present work is concerned with the verification and validation of an implementation of the eigenfracture scheme of Schmidt et al. (SIAM J Multiscale Model Simul 7:1237–1266, 2009) based on material-point erosion, which we refer to as *eigenerosion*. Eigenerosion is derived from the general eigenfracture scheme by restricting the eigendeformations in a binary sense: they can be either zero, in which case the local behavior is elastic; or they can be equal to the local displacement gradient, in which case the corresponding material neighborhood is failed, or *eroded*. When combined with a material-point spatial discretization, this scheme gives rise to *material-point erosion*, i. e., each material point can be either intact, in which case its behavior is elastic, or be completely failed—or eroded—and has no load bearing capacity. We verify the eigenerosion scheme through convergence studies for mode I fracture propagation in three-dimensional problems. By way of validation we apply the eigenerosion scheme to the simulation of combined torsion-traction experiments in aluminum-oxide bars.

A. Pandolfi (✉)
Dipartimento di Ingegneria Strutturale, Politecnico di Milano, Piazza Leonardo da Vinci 32, 20133 Milano, Italy
e-mail: pandolfi@stru.polimi.it

B. Li · M. Ortiz
Graduate Aeronautical Laboratories, California Institute of Technology, Pasadena, CA 91125, USA
e-mail: libo@caltech.edu

M. Ortiz
e-mail: ortiz@aero.caltech.edu

Keywords Meshfree approaches · Material point erosion · Eigen fracture · Max-Ent shape functions · Brittle Fracture

1 Introduction

Lagrangian meshfree methods are well-suited to a number of areas of application, such as terminal ballistics, machining, fluid-structure interaction. Lag-rangian meshfree methods offer significant advantages over competing approaches, such as purely Eulerian formulations, particle methods, purely Lagrangian formulations with continuous adaptive remeshing, arbitrary-Lagrangian–Eulerian (ALE). These competing approaches may suffer from a variety of shortcomings, for example: the introduction of large numerical diffusion errors; large discretization errors at fluid-solid interfaces; difficulties in maintaining monotonicity, positivity and in tracking state variables; spurious modes and tensile instabilities; mesh entanglement; the need to remesh or rezone arbitrary three-dimensional domains and the attendant remapping of state variables; ad-hoc transition or blending regions; difficulties in defining numerical integration rules and satisfying essential boundary conditions; unknown convergence and stability properties; and others.

A representative example of Lagrangian meshfree schemes is furnished by the Optimal-Transportation Meshfree (OTM) method of Li et al. (2010).

In the quasistatic setting of interest here, the OTM method combines: (i) Maximum-entropy (max-ent) meshfree interpolation Arroyo and Ortiz (2006) from a nodal-point set; and (ii) material-point sampling (cf., e. g., Sulsky et al. 1994) in order to track the local state of material points, carry out complex constitutive updates and perform spatial integrals. Max-ent interpolation Arroyo and Ortiz (2006) offers the advantage of being meshfree and entirely defined—essentially explicitly—by the current nodal-set positions, thus effectively sidestepping the need for continuous remeshing in simulations of unconstrained flows. In addition, max-ent interpolation satisfies a Kronecker-delta property at the boundary, which greatly facilitates the enforcement of essential boundary conditions, and has good accuracy convergence and monotonicity conditions. Because of interpolatory nature, OTM is free from the tensile numerical instabilities that plague particle methods. In dynamic problems, the OTM method additionally draws on optimal transportation concept, such as the Wasserstein distance between successive mass densities, in order to discretize the action integral in time. The optimal-transportation approach to time discretization leads to geometrically-exact updates of the local volumes and mass densities, and exact conservation properties including symplecticity, linear and angular momentum.

Many of the applications where Lagrangian meshfree schemes, such as the OTM method, are attractive involve material failure and fracture of some kind. However, there is limited experience at present concerning the simulation of fracture and fragmentation processes within the framework of meshfree interpolation schemes. Notable exceptions are the contributions in the meshfree Galerkin approximation (Belytschko et al. 1993; Lu et al. 1995; Belytschko et al. 1996), and in the smooth particle hydrodynamics method (Rabczuk and Eibl 2003; Rabczuk et al. 2004; Karekal et al. 2011). In this paper we assess the performance of a recently proposed approach to fracture, termed *eigenfracture* (Schmidt et al. 2009), within a meshfree framework. The eigenfracture scheme resorts to the classical device of *eigendeformations* (Mura 1987; Colonnetti 1917) in order to account for material fracture. To this end, the energy functional depends on two fields: the displacement field u and an eigendeformation field ε^* that describes such cracks as may be present in the body. Specifically, eigendeformations allow the displacement field to develop jumps at no cost in local elastic energy. In addition, in the eigenfracture scheme the fracture energy is set to be proportional to the volume of the ϵ-neighborhood of the support of the eigendeformation field, suitably scaled by $1/\epsilon$. The optimal crack set is obtained by minimizing the resulting energy functional with respect to both the displacement and the eigendeformation fields, subject to irreversibility constraints. We note that other two-field approximation schemes for brittle fracture, most notably the Ambrosio-Tortorelli scheme (Ambrosio and Tortorelli 1992; Braides and Defranceschi 1998), have been proposed in the past and used as a basis for numerical approximations (Bourdin and Chambolle 2000; Bourdin et al. 2000; Bourdin 2007), but the use of eigendeformations to describe brittle fracture in a variational framework does not appear to have been pursued prior to Schmidt et al. (2009). We also note that other damage regularizations of brittle fracture (Braides and Dal Maso 1997; Braides 2002; Braides and Defranceschi 1998; Negri 2005) have been proposed in the past and shown to be convergent.

In the present work, we specifically consider a meshfree approach based on maximum-entropy (max-ent) interpolation (Arroyo and Ortiz 2006) combined with material-point sampling and integration (Li et al. 2010). We confine our attention throughout to quasistatic problems. Extensions of the max-ent meshfree approach to dynamics, based on optimal-transportation theory, may be found in Li et al. (2010). In the max-ent/material-point scheme considered here, the spatial discretization is based on two sets of points: the nodal points and the material points. Specifically, the nodal points carry the information concerning the displacements, whereas the material points carry the material state, including eigendeformations. The link between material points and nodes is established through max-ent interpolation. The max-ent shape functions exhibit rapid decay and their support can be restricted to a finite range, with the result that every material point is connected to a limited number of nodes within its immediate environment.

When combined with the max-ent/material-point scheme, eigenfracture may be implemented as *material-point erosion*, i. e., the material-points can be either intact, in which case their behavior is elastic, or be completely failed—or eroded—and have no load bearing capacity. The implementation of the method, included the all-important ϵ-neighborhood construction, is exceedingly simple and applies to general

situations, possibly involving complex three-dimensional fracture patterns such as branching and fragmentation. The accuracy and convergence of the eigenerosion approach is comparable—at a much reduced implementation cost and complexity—to that of other numerical fracture schemes. We note that element erosion has been extensively used to simulate fracture in a number of areas of application, including terminal ballistics (Johnson and Stryk 1987; Belytschko and Lin 1987; Ortiz and Giannakopoulos 1990; Johnson and Stryk 1990; Whirley and Hallquist 1991; Borvik et al. 2008). However, some of these methods fail to converge or converge to the wrong limit (Negri 2003). By contrast, the eigenfracture scheme is known to properly converge to Griffith fracture (Griffith 1920) in the limit of vanishingly small mesh sizes (Schmidt et al. 2009). In particular, the local-neighborhood averaging of the energy which underlies the calculation of the effective energy-release has the effect of eliminating spurious mesh-dependencies.

We base our assessment of the method on selected verification and validation test cases. We verify the approach by means of convergence studies for mode I fracture propagation in three-dimensional plates. We additionally present a validation of the method through simulations of combined traction-torsion experiments on aluminum oxide bars (Suresh and Tschegg 1987). We find that the eigenerosion scheme indeed results in convergent approximations, both as regards crack paths as well as the attendant deformation fields and structural response. We also find that the scheme enables the simulation of exceedingly complex three-dimensional fracture patterns. The range and versatility afforded by the approach is all the more remarkable given the simplicity of its implementation.

The paper is organized as follows. In Sect. 2, we begin by formulating the problem to be approximated, namely, the problem of quasi-static crack-growth in an otherwise linear-elastic solid. We continue with brief review to the max-ent/material-point approach in Sect. 3. Then we recall briefly the eigenerosion method in Sect. 4. In Sect. 5.1 we verify the approach by means of convergence studies for mode I fracture propagation in three-dimensional plates. In Sect. 5.2 we present a validation of the method through simulations of combined traction-torsion experiments on aluminum oxide bars, taken from Suresh and Tschegg (1987). We conclude with some comments on the actual results and possible extensions in Sect. 6.

2 Variational formulation of fracture mechanics

In this section we succinctly summarize the formulation of fracture mechanics that we take as the basis for subsequent developments. We specifically follow Larsen et al. (2009) and Pandolfi and Ortiz 2012, which may be consulted for additional mathematical detail.

We consider an elastic body occupying a domain $\Omega \subset \mathbb{R}^n$, $n \geq 2$. The boundary $\partial\Omega$ of the body consists of an exterior boundary Γ, corresponding to the boundary of the uncracked body, and a collection of cracks jointly defining a crack set C. In addition, Γ is partitioned into a displacement boundary Γ_1 and a traction boundary Γ_2. The body undergoes deformations under the action of body forces, displacements prescribed over Γ_1 and tractions applied over Γ_2, subject to a contact condition on C. Under these conditions, the potential energy of the body is

$$E(u, C, t) = \begin{cases} \int_\Omega W(x, u, \nabla u)\, dx + \int_{\Gamma_2} V(x, u)\, d\mathcal{H}^{n-1}, & \text{if } [\![u]\!] \cdot \nu \geq 0, \\ +\infty, & \text{otherwise,} \end{cases} \tag{1}$$

where, here and subsequently, $\mathcal{H}^d$ is the d-dimensional Hausdorff measure,[1] ν is a unit normal to C, $[\![u]\!]$ is the displacement jump,

$$[\![u]\!] \cdot \nu \geq 0 \tag{2}$$

defines the contact constraint, W is the elastic strain energy density of the body—possibly including distributed body forces— and V is the potential of the applied tractions. The explicit dependence of E on t in (1) is meant to reflect the time dependence of the forcing, namely, the applied forces and prescribed displacements. Suppose now that the applied loads and prescribed displacements are incremented over the time interval $[t, t + \Delta t]$ and that, in response to this incremental loading, the crack set extends from $C(t)$ to $C(t + \Delta t)$. Owing to the irreversibility of fracture we must necessarily have that

$$C(t) \subset C(t + \Delta t), \tag{3}$$

i. e., the crack set must be monotonically increasing in time. Let the elastic energy increment recorded during the time increment be ΔE. Then, a classical calculation

[1] cf., e. g., Dal Maso and Toader (2002); on smooth curves, $d\mathcal{H}^1$ is the element of length; on smooth surfaces, $d\mathcal{H}^2$ is the element of area.

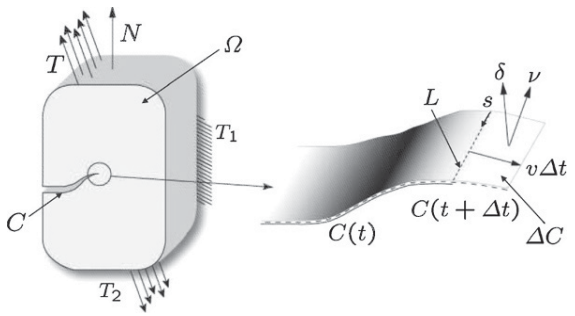

Fig. 1 Crack advancing in a body occupying a domain Ω and zoom of the crack-front region showing the crack set $C(t)$ at time t, contained in the extended crack set $C(t+\Delta t)$ at time $t+\Delta t$. During the time interval Δt the crack front L sweeps an area ΔC of unit normal ν, and propagates in the direction of the crack front velocity v

(Knees and Mielke 2008; Larsen et al. 2009) gives the rate of energy release as

$$-\dot{E} = -\lim_{\Delta t\to 0}\frac{\Delta E}{\Delta t} = \int_L G v\, d\mathcal{H}^{n-2} \tag{4}$$

where L is the crack front, Fig. 1b, v is the crack-front velocity, and

$$G = \lim_{\Delta t\to 0} \sigma\, \nu\cdot[\![u_{t+\Delta t}]\!], \quad \sigma = \partial_{\nabla u} W\,(x, u, \nabla u) \tag{5}$$

is the energetic force acting on the crack front. The identity (4) gives the rate at which energy flows to the crack front.[2] In continuum thermodynamics, the duality-pairing structure of (4) is conventionally taken to mean that the energetic force G does power, or *drives* on the crack-front velocity v. On this basis, within Osanger's general framework for inelastic processes, we may postulate the existence of a *crack-tip equation of motion* of the form

$$G = \partial\psi(v), \tag{6}$$

where ψ is a dissipation potential density per unit crack-front length. The total dissipation potential for the entire crack front finally follows by additivity as

$$\Psi(v) = \int_L \psi(v)\, d\mathcal{H}^{n-2}. \tag{7}$$

We note that the dissipation attendant to crack growth is localized to the crack front L. Under the assumption of rate-independence the dissipation potential is of the form

$$\psi(v) = G_c|v|, \tag{8}$$

which is subject to the monotonicity constraint (3). In (8), G_c is the critical energy release rate, or specific fracture energy, of the material. The assumption of rate-independence is characteristic of ideally brittle behavior and forms the basis of Griffith's theory of fracture Griffith (1920). Since the rate-independent dissipation potential $\psi(v)$, Eq. (8), is not differentiable at the origin, the equation of motion (6) must be understood in the sense of subdifferentials, namely,

$$G - G_c \le 0, \tag{9a}$$

$$v \ge 0, \tag{9b}$$

$$(G - G_c)v = 0, \tag{9c}$$

which embody Griffith's crack propagation and arrest criteria.

Because of the rate-independent nature of Griffith's criterion, the crack tracking problem can be reduced, in the spirit of the so-called *deformation theory*, to the minimization of the energy-dissipation functional Mielke and Ortiz (2007)

$$F(u, C, t) = E(u, C, t) + G_c|C| \tag{10}$$

at every time, subject to the monotonicity constraint (3), i. e.,

$$\big(u(t), C(t)\big) \in \operatorname{argmin} F(\cdot, \cdot, t), \tag{11a}$$

$$\text{subject to: } C(t_1) \subset C(t_2), \text{ whenever } t_1 < t_2. \tag{11b}$$

In (10), $|C|$ denotes the area of the crack set. Thus, the geometry of a growing crack and the corresponding equilibrium elastic field in a perfectly brittle material is obtained by jointly minimizing $F(u, C, t)$ at all times with respect to both the displacement field u and the crack set C subject to the constraint (3). In particular, the crack path results from a competition between: the elastic energy, which promotes fracture as an energy-release mechanism; the specific fracture energy, which penalizes fracture proportionally to the crack area; and the monotonicity and contact constraints, which introduce irreversibility, path dependency, hysteresis and tension-compression asymmetry.

A rigorous derivation of the deformation-theoretical formulation (11) of the crack-tracking problem may be

[2] cf. Larsen et al. (2009) for a rigorous mathematical definition of the crack front and attendant crack-front velocity.

based on energy-dissipation functionals (Mielke and Ortiz 2007), which in the present context supply a minimum principle that characterizes entire crack paths Larsen et al. (2009). Problem (11) then follows simply from by noting that, for monotonically growing brittle cracks, the dissipation (7) is an exact time-differential of $G_c|C|$, i. e.,

$$\Psi(v) = \frac{d}{dt}\left(G_c|C|\right). \tag{12}$$

Conditions for the existence of solutions of the crack-tracking problem (11), which is not guaranteed in general, may be found in Dal Maso and Toader (2002), Francfort and Larsen (2003), and Dal Maso et al. (2005).

In order to obviate the need for minimizing the energy-dissipation functional $F(u, C, t)$ with respect to the crack set C, which may be numerically cumbersome, in the framework of linearized elasticity Schmidt et al. (2009) have proposed a reformulation of the crack-tracking problem (10) in terms of *eigendeformations* ε^*, with the aid of a small parameter ϵ with units of length. In particular, the crack set is approximated as $C = \{\varepsilon^* \neq 0\}$, namely the support of the eigendeformation field, i. e., the domain over which the eigendeformation field is nonzero; and C_ϵ is the *ϵ-neighborhood* of C, i. e., the set of points that are at a distance less or equal to ϵ from C. The regularized energy-dissipation functional proposed by Schmidt et al. (2009) is

$$F_\epsilon(u, \varepsilon^*, t) = \int_\Omega W(\varepsilon(u) - \varepsilon^*)\, dV + \int_{\Gamma_2} V(x, u)\, d\mathcal{H}^{n-1} + G_c \frac{|C_\epsilon|}{2\epsilon}. \tag{13}$$

In this expression $\varepsilon(u) = \frac{1}{2}(\nabla u + \nabla u^T)$ is the the strain operator of linear elasticity and $|C_\epsilon|$ denotes the volume of the ϵ-neighborhood C_ϵ. We note that the regularized energy-dissipation functional $F_\epsilon(u, \varepsilon^*, t)$ now allows for eigendeformation fields that are spread over a volume, and thus represent a damaged volume of material. As before, the eigendeformations allow the material to relax its energy locally. The centerpiece of the approach of Schmidt et al. (2009) concerns the proper evaluation of the fracture-energy cost attendant to a distribution of eigendeformations, which is given by the last term in (13). Indeed, Schmidt et al. (2009) have shown that the regularized energy-dissipation functional F_ϵ, Eq. (13), Γ-converges to the Griffith functional F, Eq. (10), as $\epsilon \to 0$. We recall that Γ-convergence is a notion of variational convergence that implies convergence of minimizers. In particular, the scaling of the volume of the ϵ-neighborhood C_ϵ by ϵ^{-1} in the energy-dissipation functional (13) in turn penalizes the volume of the approximate crack set C, which in the limit converges to a surface.

The regularized crack tracking problem consists of minimizing the regularized energy-dissipation functional (13) for every time, subject to the monotonicity constraint (3), which now requires that the approximate crack sets grow monotonically, and to a suitable contact constraint in lieu of (2). For instance, the constraint

$$\varepsilon^* \geq 0, \tag{14}$$

first proposed by Ortiz (1985) and widely used since, can be used to enforce the contact constraint within an eigendeformation framework. Constraint (14) specifically requires that all the eigenvalues of ε^* be nonnegative, which effectively satisfy the crack closure constraint.

It bears emphasis that the net effect of the regularization of the fracture energy in (13) is to eliminate the spurious mesh-dependencies that afflict naive erosion schemes and ensure convergence of the approximations. For instance, a typical scheme consists of introducing C^0 finite-element interpolation for the displacements and piecewise constant interpolation for the eigendeformations, i. e., restricting the eigendeformations to be constant over the elements, see, e. g., Ortiz and Giannakopoulos (1990). These schemes indeed converge pointwise as the mesh size goes to zero, provided that the crack set is aligned with the mesh, as in the case of a structured mesh in a rectangular plate subjected to mode I loading, but may fail to converge otherwise Negri (2003). The reason for the lack of convergence is a geometrical one: as the crack zig-zags in accordance with the mesh in order to match the limiting crack path, it overestimates the amount of fracture energy by a geometrical factor. Negri developed converging schemes that overcome this difficulty by recourse to mesh adaption (Negri 2003, 2005) or to nonlocal averaging schemes (Negri 2005; Lussardi and Negri 2007).

3 Max-ent shape functions

The remainder of the paper is devoted to a verification and validation analysis of mesh-free approximation schemes based on the regularized crack-tracking problem just described. The spatial discretization of the energy-dissipation functional (13) considered in this work is the quasistatic version of the optimal-transportation meshfree (OTM) method developed in Li et al. (2010) for particular applications to flow of fluids and solids. The discretization is based on two sets of points: the nodal points and the material points. Thus, the nodal points x_a carry the information concerning the displacements, whereas the material points x_p carry the material state, including eigendeformations. The link between material points and nodes is established through the displacement interpolation rule:

$$u_p = \sum_{a=1}^{n} u_a N_a\left(x_p\right), \tag{15}$$

where $N_a(x)$ are conforming shape functions defined over Ω. The support of the shape functions $N_a(x)$ is expected to have a finite range, so that every material point is connected to a limited number of nodes within its immediate environment. Following Li et al. (2010), in this work we specifically use the local max-ent interpolation introduced in Arroyo and Ortiz (2006). Thus, the shape function for the node a is

$$\begin{aligned} N_a(x) &= \frac{1}{Z(x, \lambda^*(x))} \\ &\quad \times \exp\left[-\beta|x - x_a|^2 + \lambda^*(x) \cdot (x - x_a)\right], \\ a &= 1, \ldots, n, \end{aligned} \tag{16}$$

where

$$\lambda^*(x) = \arg\min_{\lambda \in \mathbb{R}^d} \log Z(x, \lambda). \tag{17}$$

The function $Z : \mathbb{R}^d \times \mathbb{R}^d \to \mathbb{R}$ is the partition function associated with the node set X, i. e.:

$$Z(x, \lambda) \equiv \sum_{a=1}^{n} \exp\left[-\beta|x - x_a|^2 + \lambda \cdot (x - x_a)\right]. \tag{18}$$

The scalar β can be chosen to be dependent on the position, e. g., related to the size of the material-point neighborhood h_p as

$$\beta_p = \gamma \frac{1}{h_p^2}, \tag{19}$$

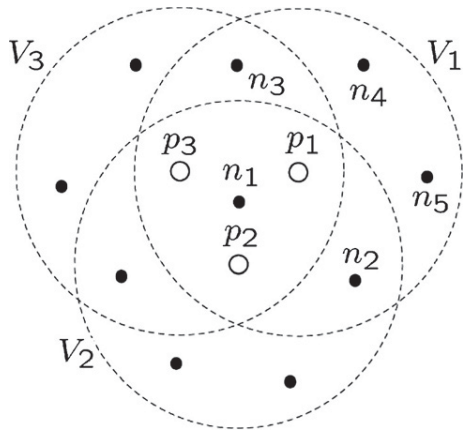

Fig. 2 Sketch of the neighborhoods of three material points, p_1, p_2 and p_3, labeled V_1, V_2 and V_3. The nodes are denoted n_i. Material point p_1 has connections to five nodes lying in V_1. Node n_1 lies inside the three neighborhoods V_k and, therefore, is connected to the three material points

where γ is a dimensionless constant that assumes positive values close to the unity. In the present applications we assume $\gamma = 0.1$. The neighborhood size h_p measures the radius of a spherical volume V_p, centered at the material point and including n_p nodal points, where the max-ent shape functions of the material point are defined. The size h_p—and therefore the number of support nodes—is not necessarily constant for all the material points. For example, in the present implementation h_p is chosen to scale with the local distance between material points. Fig. 2 illustrates the concept of h_p-neighborhood in two dimensions.

The discretization of the regularized energy-dissipation potential (13) requires the use of the shape-function derivatives, which can be found in Arroyo and Ortiz (2006). The computation of the nodal forces due to the tractions on Γ_2 may be simplified by introducing a balanced stress field τ satisfying the identities:

$$\nabla \cdot \tau = 0 \ \text{ in } \Omega, \quad \tau n = q \ \text{ on } \Gamma_2, \tag{20}$$

see Li et al. (2010), and applying the divergence theorem. By imposing the stationarity of (13), we obtain the standard nonlinear equilibrium equations. In static applications involving nonlinear material behaviors and kinematics a consistent linearization of the internal forces may be necessary. In the calculations presented here we solve the nonlinear equilibrium equations by means of an explicit dynamic relaxation algorithm Oakley and Knight (1995), which does not require computation of the tangent stiffness.

4 The eigenerosion criterion

Schmidt et al. (2009) have proved that approximations of the regularized problem converge to exact solutions of the Griffith crack-tracking problem when the mesh size and the regularization parameter ϵ tend to zero in the right order. One specific scheme that was shown to be convergent consists of approximating the displacement field by means of conventional C^0 finite-element interpolations and taking the eigendeformation field to be constant over elements but otherwise unconstrained, by using a local regularization Schmidt et al. (2009). Since the local element eigendeformations are allowed to take arbitrary values, they either are zero, in order to minimize the attendant fracture energy, or completely negate the local deformation of the element, thus rendering its elastic energy zero. Thus, in that finite element approximation scheme, the discrete crack-tracking problem is reduced to successively *failing* or *eroding* elements when the attendant elastic energy release exceeds the attendant cost in fracture energy.

A detailed algorithm for finite element erosion has been provided in Pandolfi and Ortiz (2012). The same algorithm applies to the present material-point discretization, with elements replaced by material points *mutatis mutandis*. In particular, the energy release rate attendant to the erosion of one material point can be computed explicitly, as the difference of the energies of the body before and after the erosion of the material point, or, more conveniently, it can be approximated using first-order asymptotic formulae for notches Ortiz and Giannakopoulos (1990). In addition, the fracture-energy cost is computed by recourse to the ϵ-neighborhood construction, where a small parameter ϵ with the dimension of a length is used to define a volume-like neighborhood that approximates the crack surface Pandolfi and Ortiz (2012). Finally, the contact constraint is imposed by restricting erosion to material points in a state of volumetric expansion, i. e., material points whose volume in the deformed configuration is larger than the undeformed volume.

The simulation of crack propagation requires the sequential solution of equilibrium step and material point-erosion steps. If material points are eroded, the equilibrium step needs to be repeated under the same boundary conditions in order to restore mechanical equilibrium. However, in some cases unstable crack growth may result in several material-point erosion steps at fixed external load, or on runaway material-point erosion if the problem has no solution, in the sense of existence of joint minimizers (u, C) of the energy (10). Evidently, the intermediate configurations resulting from multiple material-point erosions at fixed applied load are the result of ancillary constraints on the growth of the crack, namely, an ordering of the material points by energy-release rate and the sequential failing of material points according to that ordering. A rigorous mathematical framework for appending such ancillary quasistatic crack-growth constraints has been put forth by Larsen et al. (2010b) and Larsen (2010). An alternative regularization of the problem consists of replacing the rate-independent kinetics (12) characteristic of Griffith fracture by kinetics defined by dissipation potentials Eq. (12), with super-linear growth. This type of crack-growth kinetics has been investigated in Larsen et al. (2009) by means of energy-dissipation functionals Mielke and Ortiz (2007). Yet another—physically based— regularization of the problem consists of accounting for inertia and dynamic crack growth Bourdin et al. (2011); Li et al. (2012).

The implementation of the eigenerosion scheme into the meshfree material-point code is particularly simple. In addition to the standard arrays required by any static solver, the eigenerosion scheme requires the introduction of an array to keep track of the material points that are progressively included in the evolving ϵ-neighborhood of the crack. We recall that, according to the Γ-convergence analysis of Schmidt et al. (2009), the size ϵ of the neighborhood can be chosen freely, as long as it tends to zero more slowly than the mesh size. In the calculations presented here we simply take, based on calibration studies, $\epsilon = 2.5h_{\min}$, where $h_{\min}$ is the minimum distance between nodes.

5 Numerical examples

In this section we collect verification tests aimed at assessing the convergence characteristics of the eigenerosion scheme. We additionally present a validation example concerned with the simulation of the mixed mode I-III tests on aluminum oxide bars presented in Suresh and Tschegg (1987). This validation example showcases the ability of the eigenerosion scheme to simulate complex three-dimensional crack geometries.

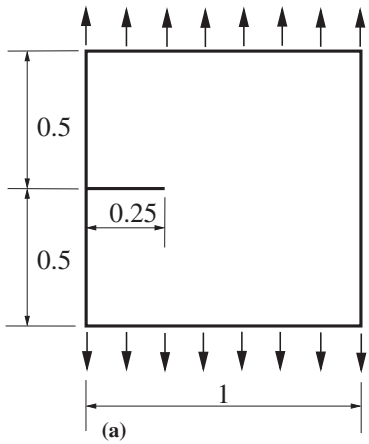

Fig. 3 Displacement boundary conditions for the square plate loaded in mode I. Edge $H = 1$, precrack $a = 0.25$, thickness $t = h_{\min}$

5.1 Edge-cracked square panel in mode I

We begin by assessing the performance of the eigenerosion scheme by means of standard numerical tests concerned with plane-strain crack growth in mode I. For purposes of comparison, we replicate the dimensionless conventions used in Pandolfi and Ortiz (2012). Specifically, we consider a square plate of size $H = 1$ containing an initial edge crack of length $a = 0.25H$ loaded in pure mode I by displacement control on the outer flanks of the plate, Fig. 3. The calculations are carried out in finite deformations for a compressible neo-Hookean material with Young's modulus $E = 1.06$, Poisson's ratio $\nu = 0.333$ and critical energy-release rate $G_c = 0.0001$. Numerical simulations are performed using a full three-dimensional code. In order to simulate two-dimensional plane-strain geometries, the boundary displacements in the third direction are constrained. In addition, we place two material points across the thickness, which is taken equal to the mesh size.

We consider three discretizations defined by the minimum distance between nodes $h_{\min}$, and labeled M1, M2 and M3, see Table 1. The distance $h_{\min}$ is taken as a basis for the definition of the ϵ-neighborhood size, leading from 3 to 4 material points in each material point ϵ-neighborhood.

The cracks for the three discretizations at the final –or at an advanced– stage of the fracture propagation are compared in Fig. 4. The crack surfaces are generated by the erosion of a single layer of material points and appear smooth and straight. The effective crack, modeled by the set of eroded material points, converges to a flat surface for $\epsilon \to 0$ following $h_{\min} \to 0$. Contour levels in Fig. 4 refer to the normal component of the Cauchy stress in the vertical direction.

Table 1 Data of the discretizations considered for the verification analysis through convergence tests in the squared prenotched plate

Discretization	Material points	Nodes	$h_{\min}$
M1	9, 600	3, 382	0.0029
M2	38, 400	13, 162	0.0014
M3	153, 600	51, 922	0.0007

Plots of global quantities per unit of thickness versus the prescribed boundary displacement demonstrating the expected mesh independency are shown in Fig. 5. In particular, Fig. 5a illustrates the global vertical reaction and Fig. 5b describes the total displacement norm $|u|_{L1}$, defined as:

$$|u|_{L1} = \int_{\Omega} |u(x)| d\Omega. \tag{21}$$

Finally, Fig. 5c shows the dependence of the strain energy E of the body on crack extension Δa. Under a prescribed boundary displacement δ the initial crack does not propagate as long as the strain energy E is less than the expenditure of fracture energy $G_c l$ necessary to break the initial ligament of length $l = 0.75$. In such situations, a null crack length $\Delta_a = 0$ is the minimizer of the functional (13). When δ equals the critical prescribed boundary displacement δ_c at which $E = G_c l$, the crack extends through the entire initial ligament with a *discrete jump* of length $\Delta a = l$, showing a sudden change of stability. At this point, the minimizer of the functional (13) is $\Delta_a = l$. We note that intermediate crack extensions $0 < \Delta a < l$ are not energy-dissipation minimizers for any prescribed boundary displacement δ and, therefore, are devoid of special meaning within the variational framework Larsen (2010).

5.2 Mixed tension-torsion experiment simulations

As a selected example of application showcasing the range and scope of the eigenerosion scheme, we proceed to simulate the combined tension-torsion

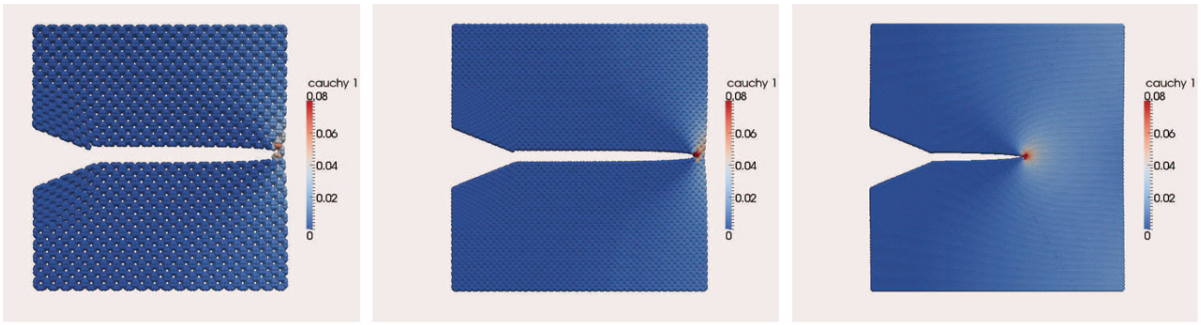

Fig. 4 Edge-crack square panel. Predicted crack paths for three meshes of increasing fineness. Contour levels refer to the normal component of the Cauchy stress in the vertical direction. **a** M1, **b** M2, **c** M3

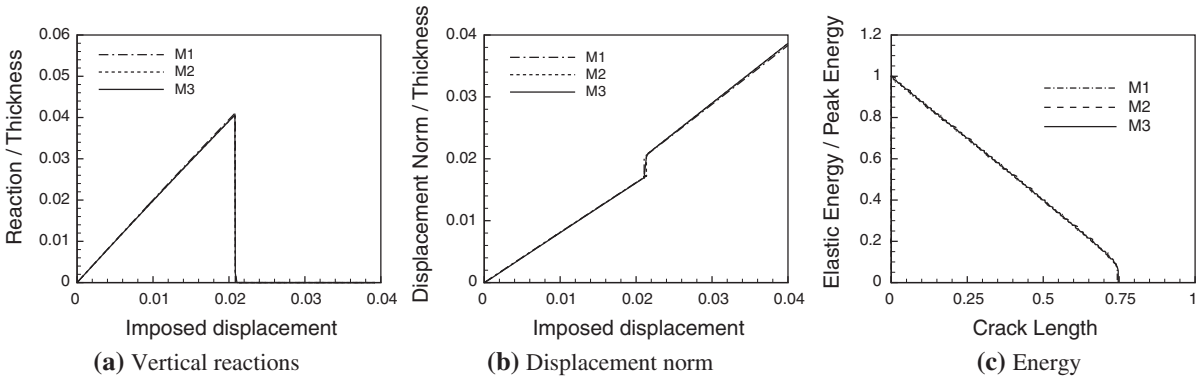

Fig. 5 Edge-cracked square panel. Dependence of: **a** global reaction force, and **b** displacement norm, on prescribed boundary displacement. **c** Dependence of the strain energy on crack length at fixed prescribed boundary displacement

experiments on aluminum oxide bar specimens with a circular notch reported by Suresh and Tschegg (1987). Fig. 6 shows the geometry of the specimen used in the experiments, with the detail of the annular pre-crack smooth notch. In the experiments the pre-crack has been sharpened by fatigue through a mode I cyclic loading in tension. To limit the computational effort, in our numerical discretization we model the central part of the specimen only, while describing accurately the notch and the fatigue crack, and apply displacement boundary conditions consistent with the experimental tension-torsion configuration, see Fig. 6. Specifically, we fix one end of the computational domain and apply a uniform axial displacement and rigid rotation about the axis at the other end. The resultants of the nodal reactions on the fixed base provide the numerical axial force and torque to be compared with the experimental data. Displacements are increased monotonically up to the onset of crack growth from notch. Thereafter, the displacements are kept constant, as in all cases the cracks grow unstably.

The experimental paper provided the material properties used in the numerical analyses, i. e., the elastic modulus $E = 345\,\text{GPa}$ and the mode I toughness $K_{Ic} = 3.35\,\text{MPam}^{1/2}$. Assuming a Poisson's coefficient $\nu = 0.3$, we derive the shear modulus $\mu = 138\,\text{GPa}$ for the neo-Hookean model. The critical energy release rate is computed through the relation

$$G_c = \frac{K_{Ic}^2}{E} \tag{22}$$

which gives $G_c = 32\,\text{N/m}$.

The three-dimensional numerical model comprises 603,996 material points and 221,191 nodes. The spatial distribution of the material points is not uniform and the discretization coarsens away from the notch,

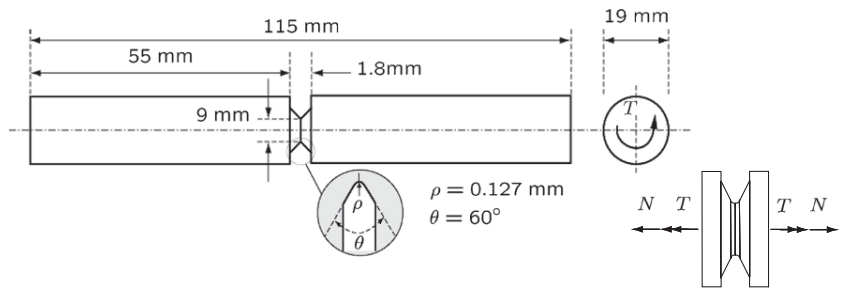

Fig. 6 Geometry of the specimen used in the experimental tests of Suresh and Tschegg (1987). The computational domain and loading used for the simulations is inset in the lower-right corner

see Fig. 7. The minimum discretization size at the notch is $h_{\min} = 0.0032$ mm. In all calculations, the max-ent interpolation parameter is set to $\gamma = 0.1$. By virtue of this choice, the range of the max-ent shape functions extends beyond nearest-neighboring nodes and, therefore, the attendant interpolation departs significantly from finite-element interpolation. An initial triangulation Fig. 7a is use in order to define the material-point set Fig. 7b and assign volumes to each material point. In order to calibrate the eigenerosion ϵ-neighborhood size we begin by performing preliminary numerical analyses in pure tension. The experimentally observed maximum axial force at failure is approximately 3,750 N Suresh and Tschegg (1987). The minimum discrepancy between the numerical and experimental axial force is found to be 5 % and to occur for $\epsilon = 2.5h_{\min}$. This value of ϵ is then used in all the subsequent calculations.

We consider three loading cases leading to different stress states at the notch: (i) pure tension or mode I loading; (ii) mixed tension—torsion or mixed-mode I–III loading, and (iii) pure torsion or mode III loading. In all cases, failure occurs catastrophically once the limit load is reached, in agreement with experiment. Suresh and Tschegg (1987) provide the pictures of the post-mortem crack surfaces for different specimens, included the tension—pure mode I—and torsion—pure mode III—cases. In the pure-tension case, the fracture surface appears flat and smooth. In all other cases, the fracture surfaces exhibit a striking saw-toothed pattern forming inclined surfaces akin to *petals*. This orderly *petal structure* breaks down in the central part of the specimen. The sharpness of the petal structure, as well as the failure load, increase with the magnitude of applied torque.

Figures 8, 9, and 10 show the aspect of the numerically computed crack surfaces for the three simulations, at one of the last stages of the fracture process. On the left side of each figure, the fracture surface is visualized by the collection of the eroded material points. In this representation, the eroded material points are located in proximity of—and *trace*—the crack surface. By contrast, on the right side of the figure we show the structure of the crack surface as obtained by means of a rendering procedure based on averaging and smoothing the positions of the eroded material points and on spline approximation (cf. Alliez et al. 2007; Mullen et al. 2010). This *postprocessing construction* aims to determine a smooth surface, which may then be identified with the crack set, that is as close as possible to the failed material-point set while costing the same amount of fracture energy. Thus, whereas eigenerosion supplies a volume approximation of the crack set, the postprocessing construction effectively reverses that approximation and provides a sharp surface representation of the crack set. A projection of the crack surfaces is additionally shown at the bottom of the figures in order to visualize the complex crack front.

It may be seen from the figures that the pure-traction case is predicted to produce a flat crack surface, whereas the pure-torsion case is predicted to result in a periodic petal structure that breaks down in the central part, in agreement with experiment. In addition, the mixed-mode case generates less sharp petals that converge smoothly towards the center of the specimen, also in agreement with experiment. The precise fractography predicted by the calculations cannot be compared quantitatively with experiment, since the original publication does not report quantitative fractographic measurements. This limitation notwithstanding, a qualitative comparison can be performed in terms of the observed number of petals, to wit: eight petals in pure torsion and seven larger petals in the mixed-mode case. Remarkably, the calculations predict exactly the same number of petals in both cases, cf. Figs. 9 and 10.

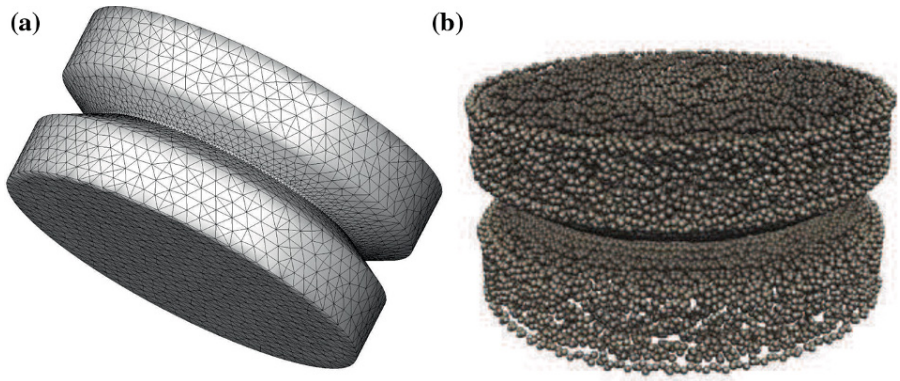

Fig. 7 Mixed-Mode tests of Suresh and Tschegg (1987). Computational model consisting of 603,996 material points and 221,191 nodes. Note the strong refinement at the notch. **a** Initial triangulation of the nodal set used to define the material-point set. **b** Visualization of the resulting material-point set

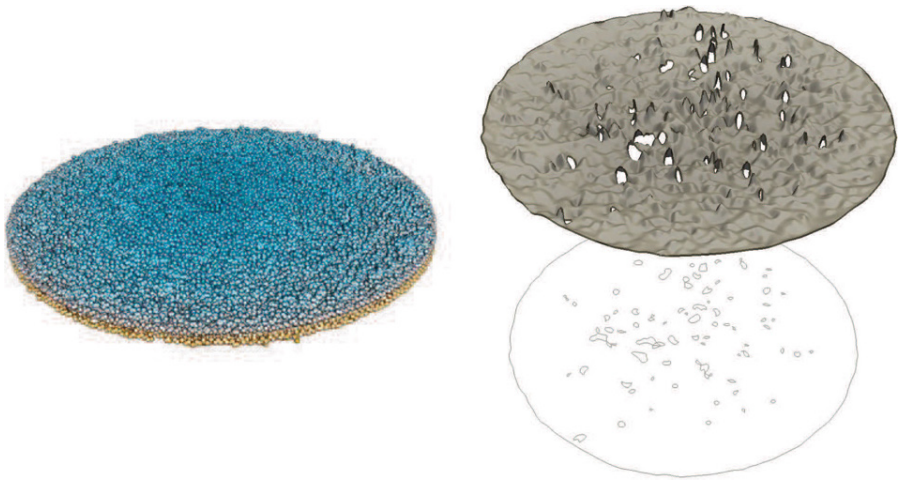

Fig. 8 Simulation of the mixed-mode tests of Suresh and Tschegg (1987), pure-tension case. *Left*: failed material-point set. *Right*: reconstructed crack surface

Further insight into the formation of complex fractographies in the pure torsion and mixed-mode experiments and simulations may be derived from stability analyses. Thus, in keeping with observation, our simulations describe the segmentation of the initially flat annular crack into daughter cracks that rotate progressively towards the direction of maximum tensile stress. Subsequently, the axial symmetry of the test forces the cracks to merge in the central part of the specimen. As observed experimentally in other geometries, mode I-III cracks often propagate unstably by the formation of inclined facets, steps and self-similar branching patterns. Stability analyses of mode I-III crack growth that shed light into such observations may be found, e. g., in (Xu et al. 1994; Movchan 1998; Lazarus et al. 2001; Lin et al. 2010; Leblond et al. 2011). These analyses reveal the existence of a critical stress intensity factor ratio K_{III}/K_I, dependent on Poisson's ratio, that separates stable and unstable planar crack growth (Xu et al. 1994; Movchan 1998; Leblond et al. 2011). Thus, for sufficiently small, respectively large, K_{III}/K_I ratio planar crack growth is stable, respectively unstable. The stress-intensity ratio corresponding to the mixed-mode test under consideration here is $K_{III}/K_I \approx 3$, which is greatly in excess of the stability limit for $\nu = 0.333$. Under these conditions, planar crack growth is unstable and the crack may indeed be expected to grow out of the plane and form complex patterns, as predicted by our calculations.

6 Summary and concluding remarks

We have described a meshfree material-point approximation method for the numerical simulation of brittle fracture propagation. The approach is based on the combination of: meshfree max-ent interpolation (Arroyo and Ortiz 2006); material-point sampling and integration (Li et al. 2010); and a convergent material-point erosion method based on the concept of eigendeformations (Schmidt et al. 2009; Pandolfi and Ortiz 2012). Specifically, the crack set is approximated by

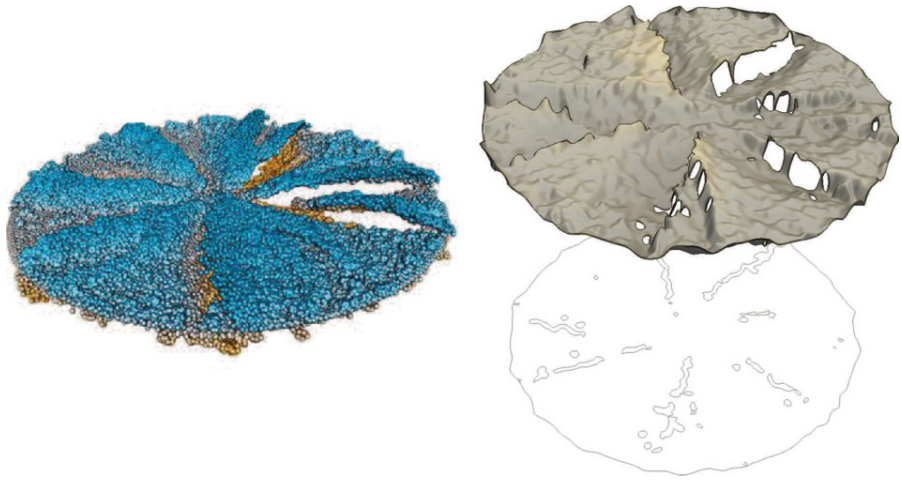

Fig. 9 Simulation of the mixed-mode tests of Suresh and Tschegg (1987), mixed tension-torsion case. *Left*: failed material-point set. *Right*: reconstructed crack surface

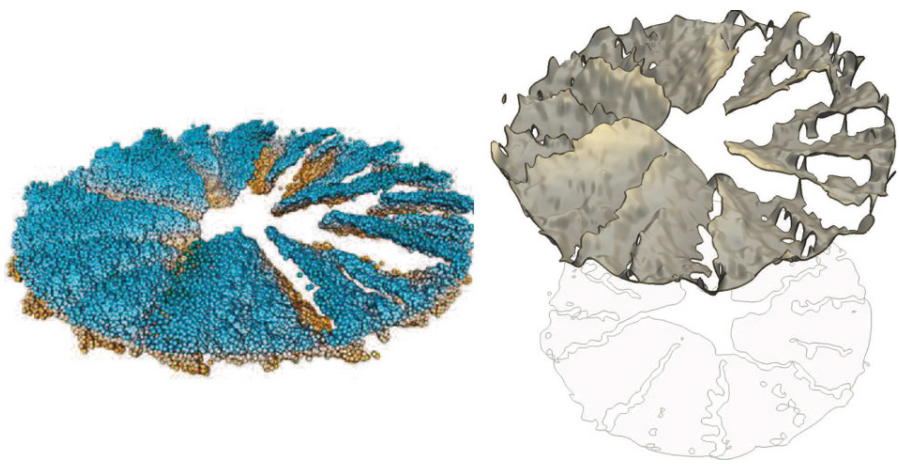

Fig. 10 Simulation of mixed-mode tests of Suresh and Tschegg (1987), pure-torsion case. *Left*: failed material-point set. *Right*: reconstructed crack surface

means of eigendeformations, which enable the material to develop displacement jumps at no cost of local elastic energy. In the implementation developed in this work, which we term *eigenerosion*, we compute the energy-release rate attendant to the failure of one material point by means of an ϵ-neighborhood construction. This construction averages the elastic energy over a length scale ϵ intermediate between the mesh size and the size of the body. In this manner, the details of the mesh are averaged over and the scheme results in mesh-insensitive—and ultimately convergent—crack paths and fracture energies. The overall convergence of the method is clearly apparent in benchmark tests such as crack initiation and growth in an edge-crack panel. The range and scope of the method has been demonstrated through the simulation of the combined torsion-traction experiments of Suresh and Tschegg (1987). The ability of eigenerosion to predict the salient features of the complex crack patterns that arise in those experiments is remarkable.

As already noted, the algorithm presented here is capable of tracking the propagation of both stable and unstable cracks. For unstable cracks, by ordering the material points by energy-release rate and failing them sequentially in accordance with that ordering, the algorithm provides crack-growth paths joining two consecutive stable crack configurations or representing runaway unstable crack growth. There exist at present rigorous mathematical approaches for understanding possibly-unstable quasistatic crack-growth in brittle solids (Larsen et al. 2009, 2010b; Larsen 2010). Whereas the present approach appears to be predictive on the basis of direct comparisons with experiment, a firm mathematical grounding of numerical crack-tracking algorithms remains to be established and is greatly to be desired.

In closing, we additionally remark that the present approach may be made extensive to inelastic behavior, including plasticity, by recourse to variational constitutive updates (Ortiz and Stainier 1999; Yang et al. 2006). Thus, variational updates provide well-defined incremental energies that combine both internal energy and dissipation. The incremental energies can in turn be used in order to define the driving force for fracture in the presence of inelasticity (Li et al. 2012).

Acknowledgments The renderings of crack surfaces presented in this paper were performed by Dr. Santiago Lombeyda and are gratefully acknowledged. The authors gratefully acknowledge the support of the Department of Energy National Nuclear Security Administration under Award Number DE-FC52-08NA28613 through Caltech's ASC/PSAAP Center for the Predictive Modeling and Simulation of High Energy Density Dynamic Response of Materials.

References

Alliez P, Cohen-Steiner D, Tong Y, Desbrun M (2007) Voronoi-based variational reconstruction of unoriented point sets. In: Belyaev A, Garland M, (eds) Eurographics symposium on geometry processing

Ambrosio L, Tortorelli VM (1992) On the approximation of free discontinuity problems. Boll Un Mat Ital B 7:105–123

Arroyo M, Ortiz M (2006) Local maximum-entropy approximation schemes: a seamless bridge between finite elements and meshfree methods. Int J Numer Methods Eng 65:2167–2202

Belytschko T, Krongauz T, Organ D, Fleming M, Krysl P (1996) Meshless methods: an overview and recent developments. Comput Methods Appl Mech Eng 139(3):3–47

Belytschko T, Lin J (1987) A three-dimensional impact-penetration algorithm with erosion. Comput Struct 25:95–104

Belytschko T, Lu YY, Gu L (1993) Crack propagation by element free galerkin methods. In: Advanced computational methods for material modeling, AMD-ASME, vol 180. p 191

Borvik T, Hopperstad OS, Pedersen KO (2008) Quasi-brittle fracture during structural impact of AA7075-T651 aluminum plates. Int J Impact Eng 37:537–551

Bourdin B (2007) Numerical implementation of the variational formulation of brittle fracture. In: IUTAM symposium on discretisation methods for evolving discontinuities. IUTAM Bookseries, Lyon, pp 381–393

Bourdin B, Chambolle A (2000) Implementation of an adaptive finite element approximation of the Mumford-Shah functional. Numer Math 85:608–646

Bourdin B, Francfort GA, Marigo JJ (2000) Numerical experiments in revisited brittle fracture. J Mech Phys Solids 48:797–826

Bourdin B, Larsen CJ, Richardson CL (2011) A time-discrete model for dynamic fracture based on crack regularization. Int J Fract 168(2):133–143

Braides A (2002) Γ-convergence for beginners. Oxford University Press, Oxford

Braides A, Dal Maso G (1997) Nonlocal approximation of the mumford-shah functional. Calc Var Partial Differ Equ 5:293–322

Braides A, Defranceschi A (1998) Homogenization of multiple integrals. Claredon Press, Oxford

Colonnetti G (1917) Su certi stati di coazione elastica che non dipendono da azioni esterne. Rendiconti dell'Accademia dei Lincei, Giugno, pp 43–47

Dal Maso G, Francfort GA, Toader R (2005) Quasistatic crack growth in nonlinear elasticity. Arch Ration Mech Anal 176(2):165–225

Dal Maso G, Toader R (2002) A model for the quasi-static growth of brittle fractures: Existence and approximation results. Arch Ration Mech Anal 162(2):101–135

Francfort GA, Larsen CJ (2003) Existence and convergence for quasi-static evolution in brittle fracture. Commun Pure Appl Math 56:1465–1500

Griffith AA (1920) The phenomena of rupture and flow in solids. Philos Trans R Soc Lond 18:16–98

Johnson GR, Stryk RA (1987) Eroding interface and improved tetrahedral element algorithms for high velocity impacts in three dimensions. Int J Impact Eng 5:414–427

Johnson GR, Stryk RA (1990) User instruction for the 1990 version of the combined (1D, 2D, 3D) EPIC code. Technical report DE-AC04-87AL-42550, DARPA

Karekal S, Das R, Mosse L, Cleary PW (2011) Application of a mesh-free continuum method for simulation of rock caving processes. Int J Rock Mech Min Sci 5:339–361

Knees D, Mielke A (2008) Energy release rate for cracks in finite-strain elasticity. Adv Math Sci Appl 31:501–528

Larsen CJ (2010) Epsilon-stable quasi-static brittle fracture evolution. Commun Pure Appl Math 63(5):630–654

Larsen CJ (2010) Epsilon-stable quasi-static brittle fracture evolution. Commun Pure Appl Math 63:630–654

Larsen CJ, Ortiz M, Richardson CL (2009) Fracture paths from front kinetics: Relaxation and rate-independence. Arch Ration Mech Anal 193:539–583

Larsen CJ, Ortner C, Suli E (2010b) Existence of solutions to a regularized model of dynamic fracture. Math Models Methods Appl Sci 20(7):1021–1048

Lazarus V, Leblond J-B, Mouchrif S-E (2001) Crack front rotation and segmentation in mixed mode I+III or I+II+III. Part II: Comparison with experiments. J Mech Phys Solids 49:1421–1443

Leblond J-B, Karma A, Lazarus V (2011) Theoretical analysis of crack front instability in mode I+III. J Mech Phys Solids 59:1872–1887

Li B, Habbal F, Ortiz M (2010) Optimal transportation meshfree approximations schemes for fluid and plastic flows. Int J Numer Methods Eng 83(12):1541–1579

Li B, Kadane A, Ravichandran G, Ortiz M (2012) Verification and validation of the optimal-transportation meshfree (OTM) simulation of terminal ballistics. Int J Impact Eng 42:25–36

Lin B, Mear ME, Ravi-Chandar K (2010) Criterion for initiation of cracks under mixed-mode I+III loading. Int J Fract 165:175–188

Lu YY, Belytschko T, Tabbara M (1995) Element-free Galerkin method for wave propagation and dynamic fracture. Comput Methods Appl Mech Eng 126:131–153

Lussardi L, Negri M (2007) Convergence of non-local finite element energies for fracture mechanics. Numer Funct Anal Optim 28:83–109

Mielke A, Ortiz M (2007) A class of minimum principles for characterizing the trajectories and the relaxation of dissipative systems. ESAIM COCV, (in press)

Movchan AB, Gao H, Willis JR (1998) On perturbations of plane cracks. Int J Solids Struct 35:3419–3453

Mullen P, de Goes F, Desbrun M, Cohen-Steiner D, Alliez P (2010) Signing the unsigned: Robust surface reconstruction from raw pointsets. In: Sorkine O, Lévy B (eds) Eurographics symposium on geometry processing 2010

Mura T (1987) Micromechanics of defects in solids. Kluwer, Dordrecht

Negri M (2003) Finite element approximation of the Griffith's model in fracture mechanics. Numer Math 95(4):653–687

Negri M (2005) A discontinuous finite element approximation of free discontinuity probems. Adv Math Sci Appl 15: 283–306

Negri M (2005) A non-local approximation of free discontinuity problems in SBV and SBD. Calc Var Partial Differ Equ 25:33–62

Oakley DR, Knight NFJr. (1995) Adaptive dynamic relaxation algorithm for non-linear hyperelastic structures. Comput Methods Appl Mech Eng 126:67–89

Ortiz M (1985) A constitutive theory for the inelastic behavior of concrete. Mech Mater 4:67–93

Ortiz M, Giannakopoulos AE (1990) Crack propagation in monolithic ceramics under mixed mode loading. Int J Fract 44:233–258

Ortiz M, Stainier L (1999) The variational formulation of viscoplastic constitutive updates. Comput Methods Appl Mech Eng 171: 419–444

Pandolfi A, Ortiz M (2012) An eigenerosion approach to brittle fracture. Int J Numer Methods Eng Online First: 1–21

Rabczuk T, Eibl J (2003) Simulation of high velocity concrete fragmentation using SPH/MLSPH. Int J Numer Methods Eng 56:1421–1444

Rabczuk T, Eibl J, Stempniewski L (2004) Numerical analysis of high speed concrete fragmentation using a meshfree lagrangian method. Eng Fract Mech 71:547–556

Schmidt B, Fraternali F, Ortiz M (2009) Eigenfracture: an eigendeformation approach to variational fracture. SIAM J Multiscale Model Simul 7:1237–1266

Sulsky D, Chen Z, Schreyer HL (1994) A particle method for history–dependent materials. Comput Methods Appl Mech Eng 118:179–196

Suresh S, Tschegg EK (1987) Combined Mode I-Mode I11 fracture of fatigue-precracked Alumina. J Am Ceram Soc 70:726–733

Whirley RG, Hallquist JO (1991) DYNA-3D User manual. Technical Report Technical Report UCRL-MA-107254, Lawrence Livermore National Laboratory

Xu G, Bower AF, Ortiz M (1994) An analysis of non-planar crack growth under mixed mode loading. Int J Solids Struct 31:2167–2193

Yang Q, Stainier L, Ortiz M (2006) A variational formulation of the coupled thermo-mechanical boundary-value problem for general dissipative solids. J Mech Phys Solids 54(2):401–424

DOI 10.1007/978-3-319-04397-5_3
Reprinted from *International Journal of Fracture*, DOI 10.1007/s10704-012-9795-y

ORIGINAL PAPER

Crack front perturbations revisited

J. R. Willis

Received: 5 October 2012 / Accepted: 27 November 2012 / Published online: 11 December 2012

Abstract The problem of the in-plane dynamic perturbation of a crack propagating with a front that is nominally straight is solved, to second order in the perturbation. The method of approach is a streamlined and generalized version of that previously applied to first order by the author and co-workers. It emerges, however, that the analysis at second order requires for its consistency the introduction of a new singular term, of a type not present at first order. The analysis is restricted to the case of Mode I loading, for clarity of exposition. It is carried out at a level of generality that incorporates viscoelastic response as well as propagation in a "vertically stratified" medium including, as a special case, propagation in a slab of finite thickness. For illustration, the general solution is specialized to the case of a stationary crack in an infinite elastic medium and agreement with a solution recently developed by methodology that is specific to the static case is confirmed.

Keywords Crack dynamics · Crack front perturbation · Viscoelastic response

J. R. Willis (✉)
Centre for Mathematical Sciences, Wilberforce Road, CB3 0WA Cambridge, United Kingdom
e-mail: J.R.Willis@damtp.cam.ac.uk

1 Introduction

The author and co-workers over a period of years solved a variety of problems involving the dynamic perturbation of a propagating crack (see e.g. Movchan and Willis 1995; Willis and Movchan 1995, 1997, 2007; further references are given later). During the course of this extended work, the methodology became increasingly refined and the purpose now is to summarise the approach that at the present time appears to be optimal. Virtually all of the previous work was devoted just to the first-order perturbation. Perturbation to higher order in fact requires the introduction of terms different in character (and not needed) at first order. This is exposed by developing the perturbation solution explicitly to second order, showing the way, in principle, to obtaining the solution to any order. The exposition is kept as simple as possible, by restricting attention to in-plane perturbation of a crack, propagating under Mode I loading. In general, the cracked medium can be a slab, occupying the domain

$$D = \{\mathbf{x} : -\infty < x_1, x_2 < \infty, -h < x_3 < h\} \qquad (1.1)$$

subjected to loading which in the absence of the crack would generate the stress field $\sigma_{ij}^A(\mathbf{x}, t)$ and corresponding displacement field $u_i^A(\mathbf{x}, t)$. The crack occupies the surface

$$S_\varepsilon = \{\mathbf{x} : -\infty < x_1 < Vt + \varepsilon\phi(x_2, t), \quad -\infty < x_2 < \infty,\ x_3 = 0\}. \qquad (1.2)$$

The more general case, involving out-of plane perturbation, would define the perturbed crack to lie on the surface $x_3 = \varepsilon\psi(x_1, x_2)$ but here $\psi \equiv 0$ is assumed. Out-of-plane perturbation was first treated by Willis and Movchan (1997) but see also Willis (1999) for a correction. Propagation in an elastic slab was addressed by Movchan et al. (2005). The stress and displacement fields in the presence of the crack are denoted σ_{ij}, u_i. They respond to the same external loading as σ^A_{ij}, u^A_i but, in addition, correspond to zero tractions on the surfaces of the crack and display a discontinuity in displacement across the crack. Thus, the difference fields $\sigma_{ij} - \sigma^A_{ij}$, $u_i - u^A_i$ satisfy the equations of motion with zero body force, together with homogeneous boundary conditions on the boundary of D (excluding S_ε), while on S_ε,

$$\sigma_{i3} - \sigma^A_{i3} = -\sigma^A_{i3},\ -\infty < x_1 < Vt + \varepsilon\phi(x_2, t),\quad x_3 = \pm 0. \tag{1.3}$$

The medium is assumed to be homogeneous or, more generally, to be vertically stratified, with properties only varying with x_3, and it can be linearly viscoelastic, with time-harmonic moduli $C_{ijkl}(\omega)$ at radian frequency ω. First-order perturbation of a crack in an infinite viscoelastic medium has been treated by Woolfries and Willis (1999), Woolfries et al. (2002), Movchan and Willis (2001, 2002).

Now introduce the Green's function G^+_{ij} defined for the medium occupying $x_3 > 0$, with traction boundary conditions applying on $x_3 = 0$ and the same types of conditions as those that define σ^A_{ij} and u^A_i, and σ_{ij} and u_i, on $x_3 = h$.[1] It follows that the difference fields satisfy, on $x_3 = 0$, the relation

$$u_i - u^A_i = -G^+_{ij} * (\sigma_{3j} - \sigma^A_{3j}), \tag{1.4}$$

the convolution being with respect to x_1, x_2 and t. Similarly, for the region $x_3 < 0$, on the boundary $x_3 = 0$,

$$u_i - u^A_i = G^-_{ij} * (\sigma_{3j} - \sigma^A_{3j}). \tag{1.5}$$

From Eqs. (1.4) and (1.5), therefore,

$$[u_i] = -2\langle G_{ij}\rangle * (\sigma_{3j} - \sigma^A_{3j}), \tag{1.6}$$

where $[u_i]$ represents the jump in displacement across $x_3 = 0$ and $\langle G_{ij}\rangle$ is the average of G^+_{ij} and G^-_{ij}.

Specialising to Mode I loading (which implies both symmetry of the loading and of the properties of the medium), the only non-zero jump in displacement is $[u_3]$ and the only non-zero traction is σ_{33}. Calling these, respectively, $[u]_-$ and σ_+, since $[u]_- = 0$ ahead of the crack and $\sigma_+ = 0$ on the crack, it follows that these satisfy the single equation

$$[u]_- + 2G * (\sigma_+ - \sigma^A) = 0, \tag{1.7}$$

where $\langle G_{33}\rangle$ is denoted G and σ^A represents σ^A_{33}. The desired aspect of the solution is the stress intensity factor. Its deduction from relation (1.7) constitutes the main task of this work.

2 Method of solution

Before proceeding further, it is useful to change coordinates to (X, x_2, t) where

$$X = x_1 - Vt. \tag{2.1}$$

It is easy to check that, with the functions re-defined as functions of (X, x_2, t), Eq. (1.7) remains exactly the same, with the convolution now interpreted relative to the new coordinates. It is also relevant to note that, if the Fourier transform of any one of the functions is known relative to the original coordinates—for instance

$$\mathscr{F}G(\xi_1, \xi_2, \omega) = \iiint G(x_1, x_2, t)e^{i(\xi_1 x_1 + \xi_2 x_2 + \omega t)}\, dx_1 dx_2 dt, \tag{2.2}$$

then its Fourier transform relative to the new coordinates is

$$\tilde{G}(\xi_1, \xi_2, \omega) = \iiint G(X + Vt, x_2, t)e^{i(\xi_1 X + \xi_2 x_2 + \omega t)}\, dX dx_2 dt = \mathscr{F}G(\xi_1, \xi_2, \omega - V\xi_1). \tag{2.3}$$

Interpreted relative to the new coordinates, at least if $\varepsilon = 0$, Eq. (1.7) defines a problem of Wiener–Hopf type. It is helpful, therefore, to factorize G as follows:

$$G = G_- * G_+, \tag{2.4}$$

where G_- is zero for $X > 0$ and G_+ is zero for $X < 0$. Correspondingly $\tilde{G}_-$ is analytic in ξ_1 for $\mathrm{Im}(\xi_1) < 0$ and $\tilde{G}_+$ is analytic in ξ_1 for $\mathrm{Im}(\xi_1) > 0$.

The basic relation (1.7) is now expressed in the form

$$\tfrac{1}{2}(G_-)^{-1} * [u]_- + G_+ * \sigma_+ = G_+ * \sigma^A. \tag{2.5}$$

In preparation for describing the general strategy, consider first the case $\varepsilon = 0$. The convolution $G_+ * \sigma_+$ is

[1] In the case $h \to \infty$, G^+_{ij} satisfies a radiation condition so that it is composed from waves travelling away from the surface $x_3 = 0$.

a "+" function while $(G_-)^{-1} * [u]_-$ is a "−" function. It follows from (2.5) that

$$G_+ * \sigma_+ = \{G_+ * \sigma^A\}_+, \tag{2.6}$$

meaning that the right side is defined to be zero when $X < 0$. Hence, formally,

$$\sigma_+ = (G_+)^{-1} * \{G_+ * \sigma^A\}_+. \tag{2.7}$$

Similarly,

$$[u]_- = 2G_- * \{G_+ * \sigma^A\}_-. \tag{2.8}$$

Evidently, the type of singularity displayed by σ_+, as $X \to 0$, is determined by the singularity of $(G_+)^{-1}$.[2] Furthermore, the coefficient of this singularity is proportional to $\{G_+ * \sigma^A\}_+$, evaluated as $X \to 0$. In the case of viscoelasticity and subsonic V, the singularity in σ_+ is of square-root type,

$$\sigma_+ \sim K_0/(2\pi X)^{1/2} \tag{2.9}$$

and, with suitable normalization of G_+,

$$K_0 = \lim_{X\to 0} \{G_+ * \sigma^A\}_+, \tag{2.10}$$

the suffix on K_0 indicating that $\varepsilon = 0$. For "intersonic" V, a similar conclusion holds but the singularity is no longer of square-root type. The relevant analysis has been performed by Obrezanova and Willis (2003, 2008). Only subsonic V is considered from now on.

The general strategy is now outlined. The factors G_+ and G_- are hard to find but it is a routine matter to obtain their Fourier transforms; hence, working is mostly performed within the Fourier domain.

First, relation (2.5) is considered as $X \to \pm 0$. Explicitly,

$$\begin{aligned}\sigma_+ \sim\ & K(\varepsilon)/(2\pi(X-\varepsilon\phi))^{1/2} + A(\varepsilon)(X-\varepsilon\phi)^{1/2} \\ & + B(\varepsilon)(X-\varepsilon\phi)^{3/2} + \cdots + \sigma_+^*(X-\varepsilon\phi, x_2, t),\end{aligned} \tag{2.11}$$

where σ_+^* is non-singular and vanishes together with all its X-derivatives as $X \to \varepsilon\phi$. Correspondingly,

$$\begin{aligned}[u]_- \sim\ & K^u(\varepsilon)(\varepsilon\phi - X)^{1/2} + A^u(\varepsilon\phi - X)^{3/2} \\ & + B^u(\varepsilon\phi - X)^{5/2} + \cdots + u_-^*(X-\varepsilon\phi, x_2, t).\end{aligned} \tag{2.12}$$

Also,

$$\begin{aligned}\{G_+ * \sigma^A\}(X) \sim\ & \{G_+ * \sigma^A\}(0) + X\{G_+ * (\sigma^A)'\}(0) \\ & + \tfrac{1}{2}X^2\{G_+ * (\sigma^A)''\}(0) + \cdots,\end{aligned} \tag{2.13}$$

having left implicit the dependence on x_2 and t. The prime denotes differentiation with respect to X.

Next, evaluate the Fourier transform of each side, with respect to X; this transformation will be indicated with a hat symbol. Considering $X \to 0$ is equivalent to considering $\xi_1 \to \infty$. The transform of the left side of (2.5) contains the products of the transforms of the participating functions and hence involves, as $X \to 0$, the asymptotic forms of $\hat{G}_+$ and $(\hat{G}_-)^{-1}$ as $\xi_1 \to \infty$. These are easiest obtained from the corresponding asymptotic forms of the transforms with respect to all arguments:

$$\tilde{G}_+ \sim \frac{(2i)^{1/2}}{(\xi_1 + 0i)^{1/2}} \left\{1 + i\frac{\overline{Q}_1}{\xi_1 + 0i} - \frac{\overline{Q}_2}{(\xi_1 + 0i)^2}\right\} \tag{2.14}$$

$$(\tilde{G}_-)^{-1} \sim \frac{2(2i)^{1/2}(\xi_1 - 0i)^{1/2}}{\mathscr{A}(V)} \left\{1 + i\frac{\overline{R}_1}{\xi_1 - 0i} - \frac{\overline{R}_2}{(\xi_1 - 0i)^2}\right\}, \tag{2.15}$$

having chosen what will be the right normalization for $\tilde{G}_+$ and employed the asymptotic form

$$\tilde{G} \sim \frac{\mathscr{A}(V)}{2|\xi_1|} \left\{1 + i\frac{\overline{G}_1}{\xi_1} - \frac{\overline{G}_2}{\xi_1^2}\right\} \tag{2.16}$$

for $\tilde{G}$. The functions $\overline{Q}_1$ etc. depend on ξ_2 and ω. Correspondingly, Q_1 etc. depend on x_2 and t. They conform to the relations

$$\overline{G}_1 = \overline{Q}_1 - \overline{R}_1, \quad \overline{G}_2 = \overline{Q}_2 - \overline{R}_2 - \overline{R}_1(\overline{Q}_1 - \overline{R}_1). \tag{2.17}$$

Transforming (2.11) and (2.12) with respect to X gives

$$\begin{aligned}\hat{\sigma}_+ \sim\ & \left\{\frac{(i/2)^{1/2}K(\varepsilon)}{(\xi_1 + 0i)^{1/2}} + \frac{\pi^{1/2}(i)^{3/2}A(\varepsilon)}{2(\xi_1 + 0i)^{3/2}}\right. \\ & \left. - \frac{3\pi^{1/2}(i)^{1/2}B(\varepsilon)}{4(\xi_1 + 0i)^{5/2}}\right\} e^{i\varepsilon\xi_1\phi} + \hat{\sigma}_+^*,\end{aligned} \tag{2.18}$$

$$\begin{aligned}[\hat{u}]_- \sim\ & \left\{\frac{K^u(\varepsilon)\pi^{1/2}(-i)^{3/2}}{2(\xi_1 - 0i)^{3/2}} - \frac{3A^u(\varepsilon)\pi^{1/2}(-i)^{1/2}}{4(\xi_1 - 0i)^{5/2}}\right. \\ & \left. - \frac{15B^u(\varepsilon)\pi^{1/2}(-i)^{3/2}}{8(\xi_1 - 0i)^{7/2}}\right\} e^{i\varepsilon\xi_1\phi} + \hat{u}_-^*.\end{aligned} \tag{2.19}$$

Transforming (2.13) with respect to X gives

$$\begin{aligned}\widehat{\{G_+ * \sigma^A\}} \sim\ & \left\{\frac{i}{\xi_1 + 0i} - \frac{i}{\xi_1 - 0i}\right\} \{G_+ * \sigma^A\}(0) \\ & - \left\{\frac{1}{(\xi_1 + 0i)^2} - \frac{1}{(\xi_1 - 0i)^2}\right\} \{G_+ * (\sigma^A)'\}(0) \\ & - \left\{\frac{i}{(\xi_1 + 0i)^3} - \frac{i}{(\xi_1 - 0i)^3}\right\} \{G_+ * (\sigma^A)''\}(0).\end{aligned} \tag{2.20}$$

[2] If $(G_+)^{-1}$ has a singularity like X^{-s} then σ_+ has a singularity like $X^{(1-s)}$.

The formulae just presented allow the development of what amounts to the "inner limit" of relation (2.5), when $X \to 0$ (if preferred, when $X = O(\varepsilon)$). The next step is to make an "outer expansion" of this inner limit. This is done by now regarding X as fixed (and so finite) and letting $\varepsilon \to 0$. This is equivalent to taking ξ_1 fixed and letting $\varepsilon \to 0$, which means adopting the expansion (to second order in ε)

$$e^{i\xi_1\varepsilon\phi} \sim 1 + i\xi_1\varepsilon\phi - \tfrac{1}{2}(\xi_1\varepsilon\phi)^2. \tag{2.21}$$

This, evidently, is equivalent to letting $\xi_1 \to 0$, or $X \to \infty$. Relation (2.5) is an identity; the result of taking these two limits remains an identity from which the desired information can be deduced. The approach is conceptually simple but the new identity contains many terms, summarised in the "Appendix", Section 5.

3 Deductions

Now set

$$K(\varepsilon) \sim K_0 + \varepsilon K_1 + \varepsilon^2 K_2 \tag{3.1}$$

with similar expansions for $A(\varepsilon)$, $B(\varepsilon)$ and the parameters with superscript u.

Implications of the identity (2.5) will be explored, using the expressions (2.20), (5.1) and (5.2). The terms $\widehat{G_+ * \sigma_+^*}$ and $\widehat{(G_-)^{-1} * u_-^*}$ are disregarded in the first instance; they will be introduced only when strictly necessary and this will first occur at order ε^2. At order ε^0, the identity (2.5) delivers three relations, the first of which is

$$K_0\frac{i}{\xi_1+0i} - \frac{(\pi/2)^{1/2}}{\mathscr{A}(V)}K_0^u\frac{i}{\xi_1-0i} = \{G_+ * \sigma^A\}(0)\left\{\frac{i}{\xi_1+0i} - \frac{i}{\xi_1-0i}\right\}, \tag{3.2}$$

from which it follows that

$$K_0 = \frac{(\pi/2)^{1/2}}{\mathscr{A}(V)}K_0^u = \{G_+ * \sigma^A\}(0). \tag{3.3}$$

The next, considering terms containing $1/\xi_1^2$, yields

$$(\pi/2)^{1/2}A_0 + Q_1 * K_0 = -\frac{(\pi/2)^{1/2}}{\mathscr{A}(V)}[\tfrac{3}{2}A_0^u - R_1 * K_0^u] = \{G_+ * (\sigma^A)'\}(0). \tag{3.4}$$

Finally, from the terms containing $1/\xi_1^3$,

$$\tfrac{3}{2}(\pi/2)^{1/2}B_0 + (\pi/2)^{1/2}Q_1 * A_0 + Q_2 * K_0 = \frac{(\pi/2)^{1/2}}{\mathscr{A}(V)}[\tfrac{15}{4}B_0^u - \tfrac{3}{2}R_1 * A_0^u + R_2 * K_0^u] = \{G_+ * (\sigma^A)''\}(0). \tag{3.5}$$

It may be noted that (3.4), taken with (3.3) and (2.17), implies the relation

$$A_0^u = -\tfrac{2}{3}\mathscr{A}(V)[A_0 + (2/\pi)^{1/2}G_1 * K_0]. \tag{3.6}$$

Similarly,

$$B_0^u = \tfrac{2}{5}\mathscr{A}(V)[B_0 + \tfrac{2}{3}(G_1 * A_0 + (2/\pi)^{1/2}G_2 * K_0)]. \tag{3.7}$$

This provides some check on the algebra because σ_+ and $[u]_-$ satisfy the relation (1.7) which involves only the Green's function G.

Next, consider terms of order ε. The first, which is independent of ξ_1, gives

$$-\phi K_0 + \phi\frac{(\pi/2)^{1/2}}{\mathscr{A}(V)}K_0^u = 0, \tag{3.8}$$

which is true on account of (3.3). Now for the terms containing $1/\xi_1$,

$$K_1 - (\pi/2)^{1/2}\phi A_0 - Q_1 * (\phi K_0) = \frac{(\pi/2)^{1/2}}{\mathscr{A}(V)}[K_1^u + \tfrac{3}{2}\phi A_0^u - R_1 * (\phi K_0^u)] = 0. \tag{3.9}$$

The terms containing $1/\xi_1^2$ give

$$\begin{aligned}&(\pi/2)^{1/2}(A_1 - \tfrac{3}{2}\phi B_0) + Q_1 * (K_1 - (\pi/2)^{1/2}\phi A_0) - Q_2 * (\phi K_0)\\ &= -\frac{(\pi/2)^{1/2}}{\mathscr{A}(V)}[\tfrac{3}{2}A_1^u + \tfrac{15}{4}\phi B_0^u - R_1 * (K_1^u + \tfrac{3}{2}\phi A_0^u) + R_2 * (\phi K_0^u)]\\ &= 0.\end{aligned} \tag{3.10}$$

The terms at order ε that contain $1/\xi_1^3$ are incomplete through truncation of the basic expansions at just three terms. Thus, B_1 is undetermined.

Using results already obtained, the first equality in (3.9) can be expressed

$$\frac{(\pi/2)^{1/2}}{\mathscr{A}(V)}K_1^u = K_1 + \phi G_1 * K_0 - G_1 * (\phi K_0) \tag{3.11}$$

and the first equality in (3.10) gives

$$-\frac{(\pi/2)^{1/2}}{\mathscr{A}(V)}(\tfrac{3}{2}A_1^u + \tfrac{15}{4}\phi B_0^u) = (\pi/2)^{1/2}(A_1 - \tfrac{3}{2}\phi B_0) + G_1 * (K_1 - (\pi/2)^{1/2}\phi A_0) - G_2 * (\phi K_0). \tag{3.12}$$

Further reduction is possible but the relations as displayed are obtainable directly from expansion of (1.7).

Consider, finally, terms of order ε^2. The terms that contain $i\xi_1$ give

$$-\tfrac{1}{2}\phi^2 K_0 + \frac{(\pi/2)^{1/2}}{\mathscr{A}(V)}(\tfrac{1}{2}\phi^2 K_0^u) = 0, \tag{3.13}$$

which is already known to be true. Now, however, consider the terms that are independent of ξ_1. They give

$$\begin{aligned}&-\phi K_1 + \tfrac{1}{2}(\pi/2)^{1/2}\phi^2 A_0 + \tfrac{1}{2}Q_1 * (\phi^2 K_0)\\ &\quad + \frac{(\pi/2)^{1/2}}{\mathscr{A}(V)}[\phi K_1^u + \tfrac{3}{4}\phi^2 A_0^u - \tfrac{1}{2}R_1 * (\phi^2 K_0^u)]\\ &\quad + \cdots = 0,\end{aligned} \tag{3.14}$$

where the terms not shown explicitly are associated with $\{\widehat{G_+ * \sigma_+^*} + \tfrac{1}{2}\widehat{(G_-)^{-1} * u_-^*}\}$.

Equation (3.14) simplifies to

$$\tfrac{1}{2}[G_1 * (\phi^2 K_0) + \phi^2 G_1 * K_0] - \phi G_1 * (\phi K_0) + \cdots = 0. \tag{3.15}$$

It can be satisfied by assuming that σ_+^* and u_-^* have "outer" expansions (i.e. as $\varepsilon \to 0$ with X fixed or, equivalently, as $X \to \infty$ with ε fixed)

$$\sigma_+^* \sim \varepsilon^2 C^* X^{-5/2}, \quad u_-^* \sim \varepsilon^2 C^{*u}(-X)^{-3/2}. \tag{3.16}$$

Correspondingly, as $\xi_1 \to 0$,

$$\begin{aligned}&\hat{\sigma}_+^* \sim \tfrac{4}{3}\varepsilon^2 C^* \pi^{1/2}(i)^{-3/2}(\xi_1 + 0i)^{3/2},\\ &\hat{u}_-^* \sim -2\varepsilon^2 C^{*u}\pi^{1/2}(i)^{1/2}(\xi_1 - 0i)^{1/2}.\end{aligned} \tag{3.17}$$

These must be multiplied[3], respectively, by the asymptotic forms of $\hat{G}_+$, $(\hat{G}_-)^{-1}$, obtainable from (2.14), (2.15). The leading-order terms in the resulting expressions are proportional to $i\xi_1$; they do not spoil Eq. (3.13) if

$$C^{*u} = -\tfrac{2}{3}\mathscr{A}(V)C^*. \tag{3.18}$$

The complete version of Eq. (3.15) now becomes

$$\begin{aligned}&\tfrac{1}{2}[G_1 * (\phi^2 K_0) + \phi^2 G_1 * K_0]\\ &\quad -\phi G_1 * (\phi K_0) + \tfrac{8}{3}(\pi/2)^{1/2} G_1 * C^* = 0.\end{aligned} \tag{3.19}$$

[3] Stated more precisely, convolutions with respect to x_2 and t must be performed.

Thus, C^* and C^{*u} are determined. Finally, the terms of order ε^2 that contain $1/\xi_1$ give

$$\begin{aligned}&K_2 - (\pi/2)^{1/2}\phi A_1 + \tfrac{3}{4}(\pi/2)^{1/2}\phi^2 B_0\\ &\quad -Q_1 * (\phi K_1 - \tfrac{1}{2}(\pi/2)^{1/2}\phi^2 A_0)\\ &\quad +Q_2 * (\tfrac{8}{3}(\pi/2)^{1/2} C^* + \tfrac{1}{2}\phi^2 K_0)\\ &= \frac{(\pi/2)^{1/2}}{\mathscr{A}(V)}\Big\{K_2^u + \tfrac{3}{2}\phi A_1^u + \tfrac{15}{8}\phi^2 B_0^u\\ &\quad -R_1 * (\phi K_1^u + \tfrac{3}{4}\phi^2 A_0^u)\\ &\quad -R_2 * (4(\pi/2)^{1/2} C^{*u} - \tfrac{1}{2}\phi^2 K_0^u)\Big\}\\ &= 0.\end{aligned} \tag{3.20}$$

The terms of order ε^2 that contain $1/\xi_1^2$ or $1/\xi_1^3$ would require for their completion more terms in the original expansions. Thus, A_2 and B_2, as well as B_1, remain undetermined. Using results already established, the first equality in (3.20) can be expressed in the form

$$\begin{aligned}\frac{(\pi/2)^{1/2}}{\mathscr{A}(V)}K_2^u &= K_2 + \phi G_1 * K_1 - G_1 * (\phi K_1)\\ &\quad +(\pi/2)^{1/2}\{\tfrac{1}{2}[G_1 * (\phi^2 A_0) + \phi^2 G_1 * A_0] - \phi G_1 * (\phi A_0)\}\\ &\quad +\tfrac{1}{2}[\phi^2 G_2 * K_0 + G_2 * (\phi^2 K_0)] - \phi G_2 * (\phi K_0)\\ &\quad +G_2 * (\tfrac{8}{3}(\pi/2)^{1/2} C^*),\end{aligned} \tag{3.21}$$

again consistent with the fact that surface traction and displacement are related through the Green's function. It follows also that

$$\begin{aligned}K_2 = {}& Q_1 * [\phi Q_1 * (\phi K_0)] - \phi Q_1^2 * (\phi K_0) + \phi Q_2 * (\phi K_0)\\ &-\tfrac{1}{2}Q_2 * (\phi^2 K_0)\\ &+\tfrac{1}{2}(\pi/2)^{1/2} Q_1 * (\phi^2 A_0) + \tfrac{3}{4}(\pi/2)^{1/2}(\phi^2 B_0)\\ &-\tfrac{8}{3}(\pi/2)^{1/2} Q_2 * C^*,\end{aligned} \tag{3.22}$$

having substituted the relevant expressions for K_1 and A_1.

Finally, with the definitions

$$L_0 = \{G_+ * (\sigma^A)'\}|_{X=0}, \quad M_0 = \{G_+ * (\sigma^A)''\}|_{X=0} \tag{3.23}$$

and using $(3.4)_1$ and $(3.5)_1$, the result can be expressed in the form

$$\begin{aligned}K_2 = {}& Q_1 * [\phi Q_1 * (\phi K_0)] - \phi Q_1^2 * (\phi K_0)\\ &+\tfrac{1}{2}[\phi^2 Q_1^2 * K_0 - Q_1 * (\phi^2 Q_1 * K_0)]\\ &+\phi Q_2 * (\phi K_0) - \tfrac{1}{2}[Q_2 * (\phi^2 K_0) + \phi^2 Q_2 * K_0]\\ &+\tfrac{1}{2}[Q_1 * (\phi^2 L_0) - \phi^2 Q_1 * L_0] + \tfrac{1}{2}\phi^2 M_0\\ &-\tfrac{8}{3}(\pi/2)^{1/2} Q_2 * C^*.\end{aligned} \tag{3.24}$$

4 Example: infinite uniform isotropic medium

It can be shown that, for this case, on the surface $x_3 = 0$,

$$G^+_{33}(x_1, x_2, t) = G^-_{33}(x_1, x_2, t) = G(x_1, x_2, t) \quad (4.1)$$

and that, relative to the frame (x_1, x_2, t),

$$\mathscr{F}G(\xi_1, \xi_2, \omega) = \frac{(\omega^2/b^2)(\omega^2/a^2 - |\xi|^2)^{1/2}}{i\mu D(|\xi|, \omega)}, \quad (4.2)$$

where $|\xi| = (\xi_1^2 + \xi_2^2)^{1/2}$ and a, b are the speeds of dilatational and shear waves:

$$a^2 = (\lambda + 2\mu)/\rho, \quad b^2 = \mu/\rho. \quad (4.3)$$

The medium has Lamé moduli λ, μ and density ρ, and

$$D(|\xi|, \omega) = 4|\xi|^2(\omega^2/a^2 - |\xi|^2)^{1/2}(\omega^2/b^2 - |\xi|^2)^{1/2} + (\omega^2/b^2 - 2|\xi|^2)^2. \quad (4.4)$$

Then, relative to the moving frame, $\tilde{G}(\xi_1, \xi_2, \omega)$ is given by replacing ω with $\omega - V\xi_1$, as prescribed in (2.3).

It follows that, as $\xi_1 \to \infty$, $\tilde{G}$ has the expansion (2.16), with

$$\mathscr{A}(V) = \frac{2(V^2/b^2)\alpha}{\mu R(V)}, \quad (4.5)$$

where $R(V)$ is the Rayleigh discriminant

$$R(V) = 4\alpha\beta - (1 + \beta^2)^2, \quad (4.6)$$

with

$$\alpha = (1 - V^2/a^2)^{1/2}, \quad \beta = (1 - V^2/b^2)^{1/2}. \quad (4.7)$$

If the medium is viscoelastic, then a and b become functions of ω relative to the original stationary frame and functions of $\omega - V\xi_1$ relative to the moving frame. It follows immediately that

$$\overline{G}_1(\xi_2, \omega) = -i\omega\frac{\mathscr{A}'(V)}{\mathscr{A}(V)}. \quad (4.8)$$

The corresponding operator in physical space is

$$G_1* = \frac{\mathscr{A}'(V)}{\mathscr{A}(V)}\frac{\partial}{\partial t}. \quad (4.9)$$

The first dependence on x_2 comes in with G_2.

Before proceeding further, consider Eq. (3.19) for C^*: it reduces to

$$\tfrac{8}{3}(\pi/2)^{1/2}\partial C^*/\partial t = -\tfrac{1}{2}[\partial(\phi^2 K_0)/\partial t + \phi^2\partial K_0/\partial t] + \phi\partial(\phi K_0)/\partial t \equiv 0. \quad (4.10)$$

Thus, remarkably, it is consistent to take $C^* = 0$.[4] Furthermore, this conclusion would persist even if the medium were anisotropic, so long as the basic propagation is in a direction of symmetry. If the coupled Mode II-III problem were considered, even for an isotropic medium, terms analogous to C^* would at least have to be admitted. It is not known at the time of writing whether or not such terms are zero if the medium is isotropic. Detailed analysis is in progress and will be reported separately.

Having established that $C^* = 0$, for the sake of a simple illustration, the problem is pursued just in the static limit, for which there is no distinction between $\mathscr{F}G$ and $\tilde{G}$ and the variable ω is simply absent. Thus,

$$\mathscr{F}G = \tilde{G} = \frac{1 - \nu}{\mu|\xi|}, \quad (4.11)$$

where $\nu = \lambda/2(\lambda + \mu)$ is Poisson's ratio. It follows immediately that

$$\tilde{G}_+ = \frac{(2i)^{1/2}}{(\xi_1 + i|\xi_2|)^{1/2}},$$
$$(\tilde{G}_-)^{-1} = \frac{(2i)^{1/2}\mu(\xi_1 - i|\xi_2|)^{1/2}}{1 - \nu} \quad (4.12)$$

so that

$$\overline{Q}_1 = -\tfrac{1}{2}|\xi_2|, \quad \overline{Q}_2 = \tfrac{3}{8}\xi_2^2. \quad (4.13)$$

Also,

$$\overline{G}_1 = 0, \quad \overline{G}_2 = \tfrac{1}{2}\xi_2^2. \quad (4.14)$$

Taken together with (3.22), these relations suffice to complete the solution of the elastostatic problem.

Consider, finally, the particular case that σ^A depends on x_1 only so that K_0, A_0 and B_0 are constants, and take the perturbation to be

$$\varepsilon\phi(x_2) = a\cos(kx_2) \quad (4.15)$$

(so that a is a suitably small length). In this case,

$$Q_1 * \phi = \mathrm{Re}\int Q_1(x_2')e^{ik(x_2 - x_2')}\,dx_2' = -\tfrac{1}{2}|ka|\cos(kx_2), \quad (4.16)$$

since $\overline{Q}_1$ is given by $(4.13)_1$. A repeat of this type of reasoning gives

$$Q_1 * [\phi Q_1 * \phi] = \tfrac{1}{4}(ka)^2[\cos^2(kx_2) - \sin^2(kx_2)]. \quad (4.17)$$

[4] Movchan and Willis (2001) unwisely included (but did not use) some results for second-order perturbation that were derived simply by comparing terms containing what is here called K_2, without checking the consistency of the other second-order terms. Their formula is correct only because, as now established, $C^* = 0$ in the case that they considered.